

## Article

# Effect of Dy<sup>3+</sup> Ions on Structural, Thermal and Spectroscopic Properties of L-Threonine Crystals: A Visible Light-Emitting Material

João G. de Oliveira Neto<sup>1</sup>, Otávio C. da Silva Neto<sup>1</sup>, Jéssica A. O. Rodrigues<sup>1</sup>, Jailton R. Viana<sup>1</sup>,  
Alysson Steimacher<sup>1</sup>, Franciana Pedrochi<sup>1</sup>, Francisco F. de Sousa<sup>2,\*</sup> and Adenilson O. dos Santos<sup>1</sup> 

<sup>1</sup> Center for Sciences of Imperatriz, Federal University of Maranhão—UFMA, Imperatriz 65900-410, MA, Brazil; joao.gon@ufma.br (J.G.d.O.N.); otavio.csn@discente.ufma.br (O.C.d.S.N.); jessica.rodrigues@discente.ufma.br (J.A.O.R.); jailton.viana@ufma.br (J.R.V.); a.steimacher@ufma.br (A.S.); f.pedrochi@ufma.br (F.P.); adenilson.santos@ufma.br (A.O.d.S.)

<sup>2</sup> Institute of Exact and Natural Sciences, Federal University of Pará—UFPA, Belem 66075-110, PA, Brazil

\* Correspondence: ffs@ufpa.br

**Abstract:** In this study, L-threonine crystals (L-thr) containing Dy<sup>3+</sup> ions (L-thrDy5 and L-thrDy10) with varying mass concentrations (5% and 10%) were successfully synthesized using a solvent slow evaporation method. The structural properties were characterized by Powder X-ray diffraction and Rietveld refinement. The data revealed that all three samples crystallized in orthorhombic symmetry ( $P2_12_12_1$ -space group) and presented four molecules per unit cell ( $Z = 4$ ). However, the addition of Dy<sup>3+</sup> ions induced a dilation effect in the lattice parameters and cell volume of the organic structure. Additionally, the average crystallite size, lattice microstrain, percentage of void centers, and Hirshfeld surface were calculated for the crystals. Thermogravimetric and differential thermal analysis experiments showed that L-thr containing Dy<sup>3+</sup> ions are thermally stable up to 214 °C. Fourier transform infrared and Raman spectroscopy results indicated that the Dy<sup>3+</sup> ions interact indirectly with the L-thr molecule via hydrogen bonds, slightly affecting the crystalline structure of the amino acid. Optical analysis in the ultraviolet–visible region displayed eight absorption bands associated with the electronic transitions characteristic of Dy<sup>3+</sup> ions in samples containing lanthanides. Furthermore, L-thrDy5 and L-thrDy10 crystals, when optically excited at 385 nm, exhibited three photoluminescence bands centered around approximately 554, 575, and 652 nm, corresponding to the  $^4F_{7/2} \rightarrow ^6H_{11/2}$ ,  $^4F_{9/2} \rightarrow ^6H_{13/2}$ , and  $^4F_{9/2} \rightarrow ^6H_{11/2}$  de-excitations. Therefore, this study demonstrated that L-thr crystals containing Dy<sup>3+</sup> ions are promising candidates for the development of optical materials due to their favorable physical and chemical properties. Additionally, it is noteworthy that the synthesis of these systems is cost-effective, and the synthesis method used is efficient.

**Keywords:** L-threonine; Dy<sup>3+</sup> ions; structure; crystal voids; thermal and spectroscopic properties; photoluminescence



Received: 24 November 2024

Revised: 8 January 2025

Accepted: 10 January 2025

Published: 13 January 2025

**Citation:** Oliveira Neto, J.G.d.; Silva Neto, O.C.d.; Rodrigues, J.A.O.; Viana, J.R.; Steimacher, A.; Pedrochi, F.; Sousa, F.F.d.; Santos, A.O.d. Effect of Dy<sup>3+</sup> Ions on Structural, Thermal and Spectroscopic Properties of L-Threonine Crystals: A Visible Light-Emitting Material. *Quantum Beam Sci.* **2025**, *9*, 3. <https://doi.org/10.3390/qbs9010003>

**Copyright:** © 2025 by the authors.

Licensee MDPI, Basel, Switzerland.

This article is an open access article distributed under the terms and conditions of the Creative Commons Attribution (CC BY) license (<https://creativecommons.org/licenses/by/4.0/>).

## 1. Introduction

The synthesis of organic and inorganic crystals doped with lanthanide ions has seen a significant rise in interest in recent years [1,2]. The literature indicates that introducing impurities into a crystalline matrix impacts various physical properties, including morphology, crystallinity, optical, mechanical, and microstructural characteristics [3,4]. The incorporation of rare earth ions into host materials has expanded their applications in

optical and electrical sciences, enabling their use in sensors, emitters, solid-state lasers, fluorescent markers, light-emitting diodes (LEDs), and frequency converters [5,6]. Rare earth elements are known for their 4f–4f electronic transitions from excited states to ground states, which generate luminescence that spans from the ultraviolet to the infrared regions [7,8].

In this context, the trivalent dysprosium ( $\text{Dy}^{3+}$ ) ion has attracted attention from scientists due to its luminescence efficiency [9,10]. Additionally,  $\text{Dy}^{3+}$  is a strong candidate for white light generation because of its  $4f^9 \rightarrow 4f^9$  electronic transitions, which produce emission lines in the blue, yellow, and red spectral regions, corresponding to the transitions  ${}^4\text{F}_{9/2} \rightarrow {}^6\text{F}_{15/2}$ ,  ${}^4\text{F}_{9/2} \rightarrow {}^6\text{H}_{13/2}$ , and  ${}^4\text{F}_{9/2} \rightarrow {}^6\text{H}_{11/2}$ , respectively [11]. However, the intensity of the electric dipole transition  ${}^4\text{F}_{9/2} \rightarrow {}^6\text{H}_{13/2}$  is dependent on the appropriate choice of host matrix. The literature reports various studies on different dysprosium-doped crystalline and amorphous matrices that exhibit white light and other color emissions [12]. Nevertheless, the study of luminescent properties in amino acid crystals remains limited.

Several amino acids have been employed in large industrial applications due to their excellent crystalline hosting capabilities [13]. For instance, the growth and characterization of pure and doped hydrochloric L-histidine crystals with transition metals and lanthanide ions using the Shankaranarayana–Ramasamy technique have been recently reported [14–16]. Another significant example is the growth of sulfamic acid crystals containing  $\text{Ce}^{3+}$  ions, with their properties also studied using the aforementioned technique [17]. According to the literature [18–20], L-threonine (L-thr) crystallizes in an orthorhombic system with the  $P2_12_12_1$ -space group. Several studies have reported the use of this material as a crystalline matrix for doping with metals and inorganic compounds [21,22]. However, there is no research regarding the use of this amino acid as a host for  $\text{Dy}^{3+}$  lanthanide ions.

Motivated by the context, in this work, pure L-thr crystals and  $\text{Dy}^{3+}$  ions containing concentrations of 5 (L-thrDy5) and 10% (L-thrDy10) by mass were grown in the orthorhombic phase by the solvent slow evaporation method, which so far has not been reported by the literature. In addition, our research aims to analyze the physical properties of the crystals by powder X-ray diffraction (PXRD), scanning electron microscopy (SEM), Fourier-transform infrared (FT-IR) spectroscopy, Raman spectroscopy, thermogravimetric analysis (TG), differential thermal analysis (DTA), ultraviolet–visible (UV–Vis) spectroscopy, and photoluminescence studies. From the results, we verified that the L-thrDy5 and L-thrDy10 crystals can be useful for possible applications as visible light-generating devices.

## 2. Materials and Methods

### 2.1. Crystals Growth

The crystals were grown using the solvent slow evaporation method with mass ratios of 1:0 (L-thr), 0.95:0.05 (L-thrDy5), and 0.90:0.10 (L-thrDy10) for the reagents L-threonine ( $\text{C}_4\text{H}_9\text{NO}_3$ —Sigma Aldrich, Darmstadt, Germany, 99.0%) and dysprosium (III) chloride hexahydrate ( $\text{Cl}_3\text{Dy}\cdot 6\text{H}_2\text{O}$ —Sigma Aldrich, Darmstadt, Germany, 99.9%), respectively, in 40 mL of deionized water. The solutes were thoroughly homogenized using a magnetic stirrer set at 360 RPM for 5 h at a controlled temperature of 50 °C. Subsequently, the solutions were stored in an oven at 35 °C until crystal growth. The chemical reaction that describes the nucleation process of the solid phase from a saturated solution of these reagents is presented below:



After three weeks, the L-thr, L-thrDy5, and L-thrDy10 crystals were successfully obtained, exhibiting transparency and well-defined morphological facets (see Figure 1a–c).

All samples crystallized at an acidic pH of approximately 4.6 and had average dimensions of  $2.0 \times 5.0 \times 13 \text{ mm}^3$  (L-thr),  $4.0 \times 5.0 \times 17 \text{ mm}^3$  (L-thrDy5), and  $4.0 \times 5.0 \times 25 \text{ mm}^3$  (L-thrDy10), as shown in Figure 1a–c. Furthermore, it is important to highlight that the concentrations of 5% and 10% associated with  $\text{Dy}^{3+}$  impurities were chosen because higher proportions result in the formation of complexes.

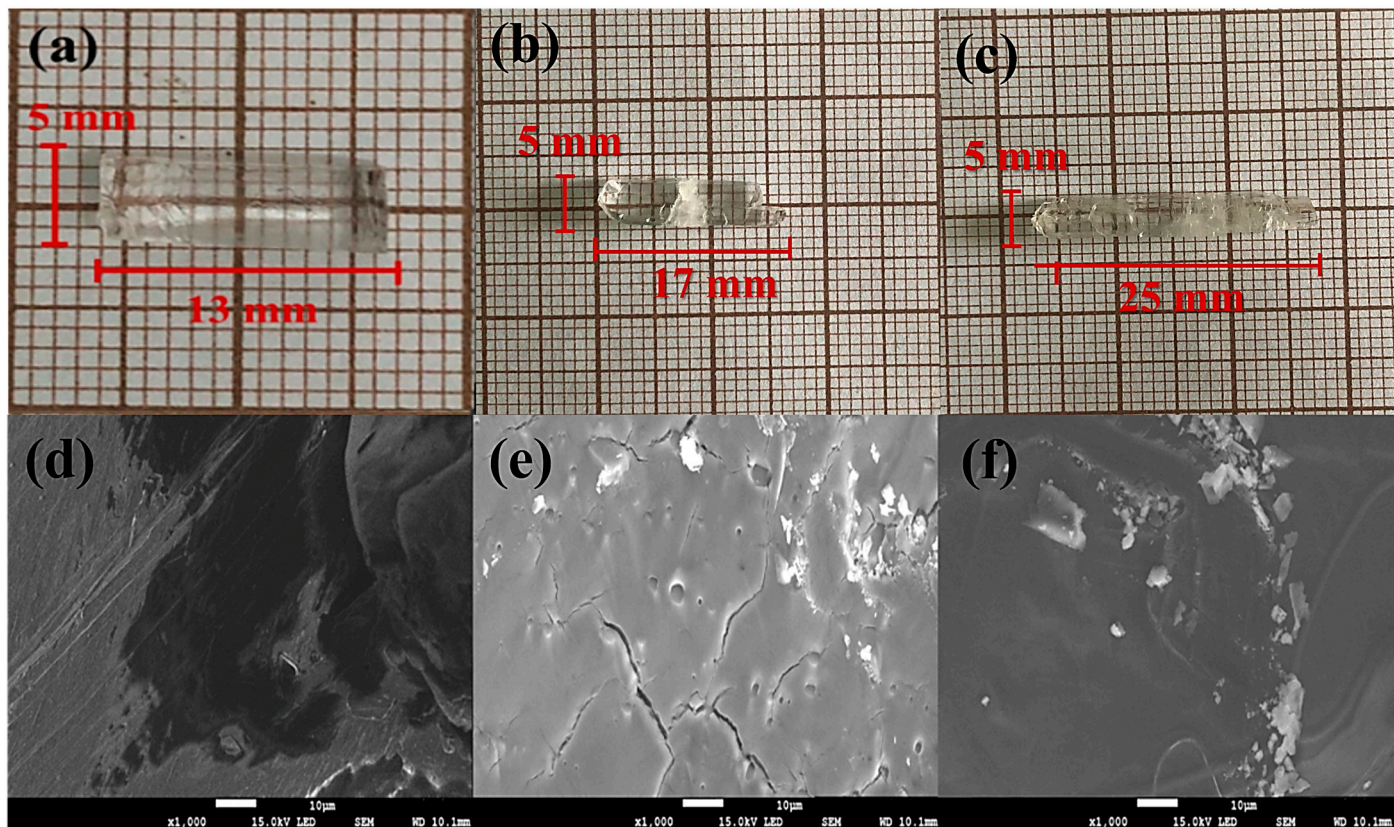


**Figure 1.** Photograph of (a) L-thr, (b) L-thrDy5, and (c) L-thrDy10 crystals. SEM micrographs of (d) L-thr, (e) L-thrDy5, and (f) L-thrDy10 samples.

## 2.2. Characterization Techniques

The surface of the crystals and the incorporation of  $\text{Dy}^{3+}$  ions into the organic matrix were analyzed using SEM. These measurements were performed with a JEOL JSM-7100F electron microscope, where the crystals were mounted on aluminum stubs with carbon tape.

The crystalline structure of the samples was characterized using a PANalytical powder diffractometer (Model: Empyrean) with  $\text{CuK}\alpha$  radiation of  $\lambda = 1.54056 \text{ \AA}$ , operating at 45 kV and 40 mA. The PXRD patterns were recorded at room temperature in the  $2\theta$  interval from  $5$  to  $45^\circ$ , with a step size of  $0.02^\circ$  and a counting time of 2 s. Furthermore, the diffractograms obtained were analyzed by Rietveld's refinement method using EXPGUI-GSAS software (Version 3.0) [23].

Thermal analysis of simultaneous TG and DTA were performed in the crystals powder using a Shimadzu DTG-60 equipment, under a nitrogen atmosphere with a flow rate of 100 mL/min. The measurements were recorded in the temperature range between 25 and  $600^\circ\text{C}$ , with a mass of approximately  $\approx 3$  to 15 mg for the three samples.

FT-IR spectra were measured at room temperature in the spectral region of  $4000\text{--}400 \text{ cm}^{-1}$  with a Bruker IR spectrophotometer (Vertex 70v), using the KBr pellet method, in which 2 mg of powdered crystals were mixed with 198 mg of KBr. This mixture was submitted to a charge of  $7 \text{ tons}\cdot\text{cm}^{-2}$  to produce a clear and homogeneous pellet. The IR absorption

spectra were carried out immediately after preparing the pellets and measured with a spectral resolution of  $4\text{ cm}^{-1}$  for 100 scans. Complementarily, measurements of Raman spectroscopy were also performed on the crystal powder through a Trivista 557 Princeton triple spectrometer. A solid-state laser with a wavelength of 633 nm (red) was used as the excitation source. The spectra were measured with an average of 5 accumulations with 90 s time for each of them and a spectral resolution of  $2\text{ cm}^{-1}$ .

UV–Vis absorbance spectra were measured in the range of 230–950 nm by a UV/VIS/NIR Thermo Scientific—Evolution 220 spectrophotometer, with a dual-beam, deuterium lamp, using quartz cuvettes with a 0.1 cm optical path. Additionally, the photoluminescence spectra in the excitation and emission regimes were performed in a Shimadzu spectrofluorometer, RF-6000, with an Xe flash lamp as the excitation source. Moreover, the emission spectrum was deconvoluted using color mathematical functions established by the Commission Internationale de l’Eclairage (CIE), in 1931, where it was possible to extract the chromaticity coordinates ( $x, y$ ) and calculate the correlated color temperature (CCT).

### 2.3. Computational Study

A computational calculation was performed using Crystal Explorer 17 software [24] to quantify the free volume of the L-thr unit cell, the surface area, and the percentage of void centers in this crystalline solid. This information allows for the identification of the insertion mechanism of  $\text{Dy}^{3+}$  ions into the structural lattice through electronic density isosurfaces. Additionally, a qualitative and quantitative study was applied to the structure using three-dimensional Hirshfeld surfaces from the same software.

## 3. Results and Discussion

### 3.1. Analysis of the Crystalline Surface and Elemental

Figure 1d–f displays SEM micrographs of the surfaces of L-thr, L-thrDy5, and L-thrDy10 crystals. The L-thr sample exhibits a smooth, uniform surface with few defects. In contrast, the samples containing impurities show various interfacial defects, including discontinuities, cracks, occlusion centers, pores, and grains of random sizes. These defects occur due to the insertion of uncommon ions ( $\text{Dy}^{3+}$ ) into the crystalline lattice of L-thr. The added impurity generates internal stresses within the crystal structure because of the size difference between the ion and the molecule of the system. As a result, defects and discontinuities are formed on the surface of the L-thrDy5 and L-thrDy10 samples. Additionally, the introduction of secondary species into organic matrices induces perturbations in the crystalline reticule. Although these perturbations are not extensive, they slightly affect the atomic periodicity and cause surface flaws.

Complementary, a semiquantitative elemental analysis conducted by energy-dispersive X-ray spectroscopy (EDXS), coupled with SEM, confirmed the presence of elements C, N, and O in all samples. Furthermore, the elements Dy and Cl were detected in the L-thrDy5 and L-thrDy10 crystals, confirming the presence of impurities in the L-thr matrix. Oliveira Neto, J.G. et al. [25] observed the same behavior for a  $\text{K}_2\text{Cu}(\text{SO}_4)_2(\text{H}_2\text{O})_6$  crystal in a thermostructural study. This is because the characteristic X-ray radiation emitted by hydrogen atoms is not strong enough to be detected by EDX sensors. It is noteworthy that light elements like H were not identified due to the sensitivity limitations of this technique for low atomic weight elements.

### 3.2. PXRD and Crystal Voids

Figure 2a shows the PXRD patterns refined by the Rietveld method for pure L-thr crystals and those containing  $\text{Dy}^{3+}$  ions. Under room conditions, all three samples crystallize in orthorhombic symmetry with the  $P2_12_12_1$ -space group, containing four molecules

per unit cell ( $Z = 4$ ). Additionally, the unit cell lattice parameters for each sample were calculated and are shown in Figure 2b and Table 1. These values agree with previously published data for L-thr crystals [26]. As observed, the L-thrDy5 and L-thrDy10 crystals exhibited a slight increase in unit cell volume ( $\approx 0.18\%$ ) compared to the L-thr crystal. This structural expansion is attributed to the increased lattice parameters of the unit cells due to the incorporation of  $\text{Dy}^{3+}$  ions into the L-thr matrix, as the dysprosium atom has a large atomic radius ( $2.31 \text{ \AA}$ ), which causes a triaxial pressure effect on the organic structure.

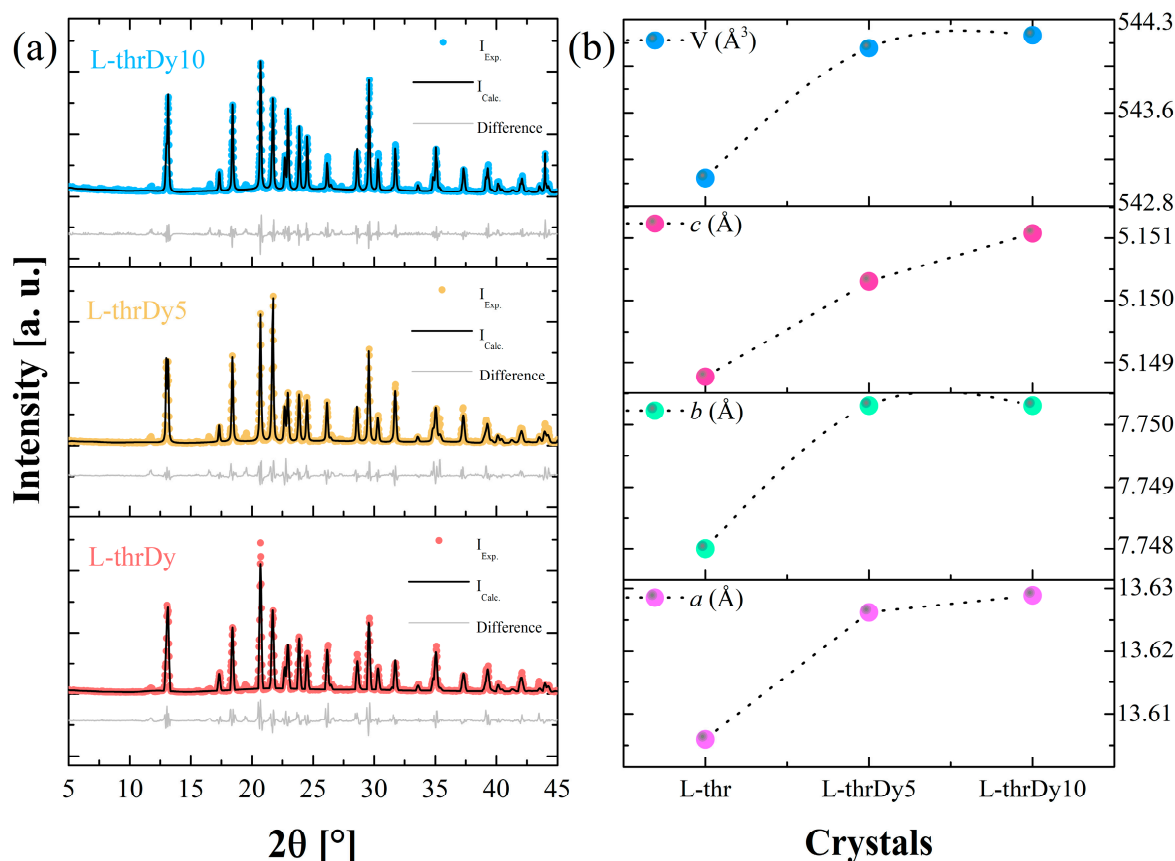


**Figure 2.** (a) Room-temperature Rietveld's refinement of the PXRD patterns for the L-thr, L-thrDy5 and L-thrDy10 crystals. (b) Lattice parameters ( $a$ ,  $b$ ,  $c$ ), and  $V$  obtained by Rietveld's refinement method.

**Table 1.** Lattice parameters, quality parameters, and structural parameters obtained for L-thr, L-thrDy5, and L-thrDy10 crystals.

Parameters	L-thr	L-thrDy5	L-thrDy10
Crystalline system	Orthorhombic	Orthorhombic	Orthorhombic
Space group	$P2_12_12_1$	$P2_12_12_1$	$P2_12_12_1$
$a$ [Å]	13.613(5)	13.628(8)	13.630(6)
$b$ [Å]	7.748(3)	7.751(3)	7.751(8)
$c$ [Å]	5.149(6)	5.151(8)	5.152(8)
$V$ [Å <sup>3</sup> ]	543.1(6)	544.1(4)	544.2(7)
$\alpha = \beta = \gamma$ [°]	90	90	90
$R_{wp}$ [%]	8.66	10.07	14.88
$R_p$ [%]	7.71	8.67	11.79
$R_e$ [%]	1.12	1.16	1.26
$S$	2.76	2.21	2.97
$D$ [nm]	43.48	41.73	40.45
$\epsilon$ [%]	0.18	0.21	0.23

It is worth noting that the concentration of Dy used (5% and 10% by mass) is low; therefore, it can be characterized as an impurity within the host matrix. Additionally, it is important to understand the centers and void percentages in the unit cell of the L-thr crystal to infer how the  $\text{Dy}^{3+}$  ions are incorporated into this structure. Figure 3 shows the voids present in the unit cell of the L-thr crystal, visualized by electron density isosurfaces (gray). According to computational calculations, the L-thr sample has a void volume of  $40.33 \text{ \AA}^3$ , corresponding to 7.42% of void spaces in the unit cell, and a surface area of  $147.49 \text{ \AA}^2$ . It was also observed that the isosurfaces are not completely enclosed around all the L-thr molecules but are open in some centers of the unit cell [27]. These regions, where interspecies interactions occur, are where the  $\text{Dy}^{3+}$  ions may be interstitially inserted and interact with the main molecule through intermolecular forces. Santana et al. [26] support this insertion mechanism, demonstrating that copper impurities ( $1.96 \text{ \AA}$ ) occupy interstitial positions in the L-thr structure.

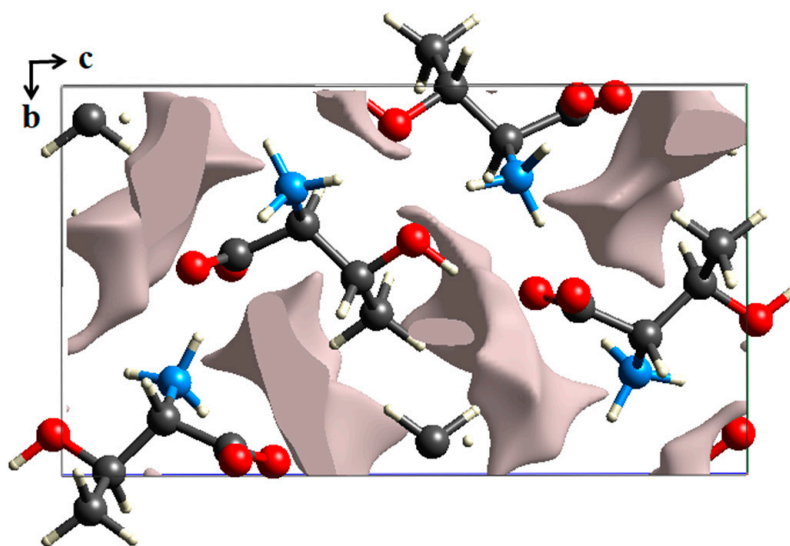


**Figure 3.** Void isosurfaces of the L-thr crystal unit cell along the  $a$ -axis. Gray circles: carbon, blue circles: nitrogen, red circles: oxygen, and white circles: hydrogen.

In order to investigate the structural distortions caused by the  $\text{Dy}^{3+}$  ions in the L-thr matrix, the average crystallite size ( $D$ ) and the lattice microstrain ( $\epsilon$ ) were calculated for the three samples based on PXRD patterns. For this, the Debye–Scherer ( $D = \frac{K \cdot \lambda}{\beta \cdot \cos \theta}$ ) and Williamson–Hall ( $\epsilon = \frac{\beta}{4 \cdot \tan \theta}$ ) relations were used [28,29], where  $K$  is the form factor ( $K = 0.9$ ),  $\lambda$  is the wavelength of X-ray ( $1.54056 \text{ \AA}$ )  $\text{CuK}\alpha$  radiation,  $\beta$  is the full width at half maximum of the diffraction peak, and  $\theta$  is the Bragg's angle. According to the calculations for the average crystallite size value, the following sequence was observed: L-thr ( $D = 43.48 \text{ nm}$ ) > L-thrDy5 ( $D = 41.73 \text{ nm}$ ) > L-thrDy10 ( $D = 40.45 \text{ nm}$ ). For the lattice microstrain, an inverse behavior was analyzed, where L-thr ( $\epsilon = 0.18\%$ ) < L-thrDy5 ( $\epsilon = 0.21\%$ ) < L-thrDy10 ( $\epsilon = 0.23\%$ ). These data indicate that the increase in the concentration of  $\text{Dy}^{3+}$  ions in the L-thr lattice induces a greater lattice microstrain. This process entails numerous defects in the crystal lattice and stress within the structure, which generates a reduction in the average crystallite size for samples containing  $\text{Dy}^{3+}$  ions.

Similar results are reported in the literature for L-thr crystals containing  $\text{Ce}^{3+}$  ions [30]. However, the L-ThrCe sample (10% by mass) showed a higher average crystallite size ( $D = 42.5 \text{ nm}$ ) and a higher lattice microstrain ( $\epsilon = 0.25\%$ ) compared to L-thr crystals containing  $\text{Dy}^{3+}$  ions. Since the cerium atom ( $2.42 \text{ \AA}$ ) has a larger atomic radius than the dysprosium atom ( $2.31 \text{ \AA}$ ),  $\text{Ce}^{3+}$  ions induce more significant defects in the L-thr structure than  $\text{Dy}^{3+}$  ions.

To provide more details on how  $\text{Dy}^{3+}$  ions interact with L-thr molecules in the unit cell of the matrix, an additional computational approach based on Hirshfeld surfaces was conducted, as presented in Figure 4. The illustrated three-dimensional map is identified in terms of the distances from a given point on the generated surface to the nearest external atom ( $d_e$ ) and internal atom ( $d_i$ ), as well as the van der Waals radius ( $r_{vdW}$ ) [31]. The surface is mapped in a color gradient associated with the intensity of each intermolecular interaction: white represents contacts equivalent to  $r_{vdW}$ , blue indicates contacts with distances greater than  $r_{vdW}$ , and red signifies contacts with distances shorter than  $r_{vdW}$ . The purple dashed lines represent the dominant intermolecular interactions in the crystal lattice. From a quantitative analysis, it was identified that the contacts present in the structure are of  $\text{H}\cdots\text{O}/\text{O}\cdots\text{H}$ ,  $\text{H}\cdots\text{H}$ ,  $\text{C}\cdots\text{H}/\text{H}\cdots\text{C}$ , and  $\text{O}\cdots\text{O}$  origin, with contribution percentages of 51.8%, 45.2%, 2.6%, and 0.4%, respectively. In other words, as  $\text{Dy}^{3+}$  ions occupy interstitial sites in the L-thr unit cell, the interaction occurs with the molecules through the H and O atoms (mapped in red) present in the  $\text{NH}_3$  (amine group),  $\text{COOH}$  (carboxyl group), and OH (hydroxyl group). Predominantly, in organic or semi-organic crystals, these detected interactions are frequently observed due to the presence of functional groups such as carbonyl, carboxyl, and hydroxyl, as also observed in the compounds dichloro-bis(theophylline)-copper(II) and nicotinamide-tetradecanoic acid [27,32].

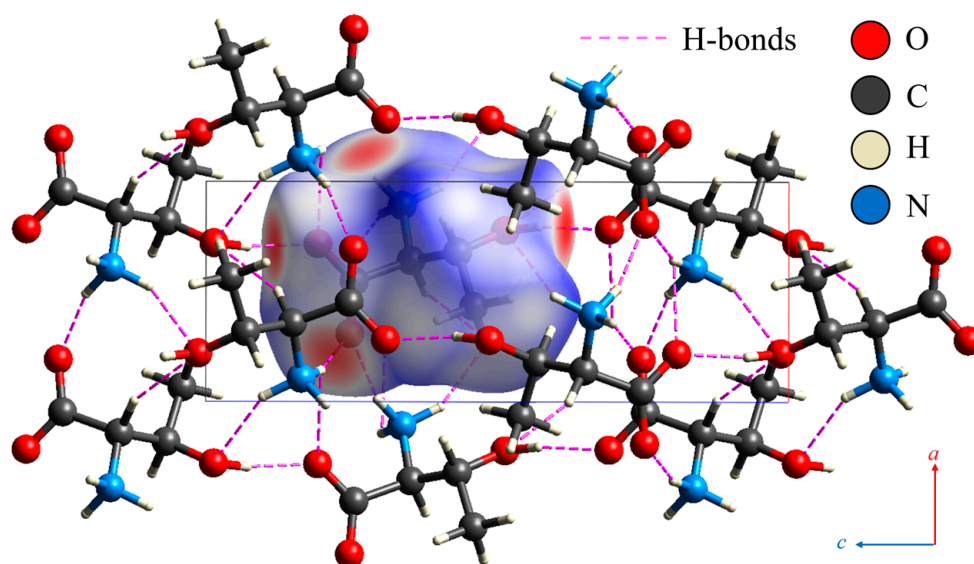


**Figure 4.** L-thr unit cell mapping the main molecule through 3D Hirshfeld surface along the  $b$ -axis. Gray circles: carbon, blue circles: nitrogen, red circles: oxygen, and white circles: hydrogen.

### 3.3. Thermal Analyses

Figure 5 presents the TG and DTA curves obtained for pure L-thr crystals and those containing  $\text{Dy}^{3+}$  ions, over the temperature range of 30 to 600 °C. Up to 210 °C, no mass loss was observed for the L-thr sample; however, the L-thrDy5 and L-thrDy10 samples showed a slight increase in thermal stability, at 212 and 214 °C, respectively. Beyond this, all crystals exhibited a significant mass loss in the TG curve up to 300 °C, indicating the thermal decomposition of the organic compounds. The DTA curve shows a sharp peak around 259–261 °C, indicating the melt-decomposition process of the crystals. Heating at this temperature causes the rupture of chemical bonds between the L-thr molecules, leading to the fragmentation of the compounds within the crystal lattice. Additionally, an endothermic event was observed between 300 and 550 °C for the L-thrDy10 crystal, which may be related to the oxidation process of  $\text{Dy}^{3+}$  ions in the structure [33]. The results

show that  $\text{Dy}^{3+}$  ions (up to 10% by mass) do not directly affect the thermal stability of the L-thr crystal.

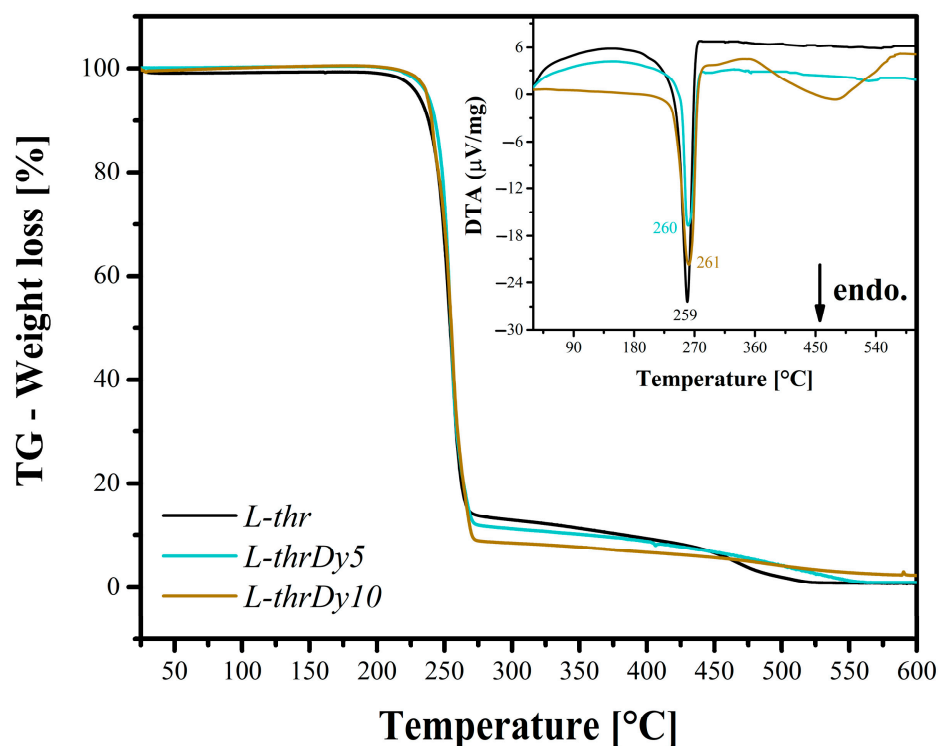


**Figure 5.** TG and DTA curves of L-thr, L-thrDy5 and L-thrDy10 crystals.

### 3.4. FT-IR Spectroscopy Studies

Figure 6 presents the FT-IR absorption spectra for L-thr, L-thrDy5, and L-thrDy10 powdered crystals, recorded under vacuum conditions in the 400 to 4000  $\text{cm}^{-1}$  range. As observed, there are no major differences between the three spectra, reinforcing the hypothesis suggested by the PXRD data that  $\text{Dy}^{3+}$  ions likely occupy interstitial centers within the crystal structure. These ions bind to the atomic arrangement through lower-energy peripheral bonds, such as hydrogen bonds or London dispersion forces. This process does not cause significant structural changes but does alter the intensities of the characteristic bands of functional groups involved in intramolecular bonds, such as the  $\text{NH}_3^+$  and  $\text{COO}^-$  groups. Furthermore, the presence of interstitial ions in the host matrix can increase the strength of the hydrogen bonds, which are crucial for the formation of the crystal structure [34,35].

In the high wavenumber region, the low-intensity vibrational modes located at 3167, 2976, and 2872  $\text{cm}^{-1}$  (L-thr); 3170, 2975, and 2871  $\text{cm}^{-1}$  (L-thrDy5); and 3167, 2975, and 2873  $\text{cm}^{-1}$ , are associated with  $\text{NH}_3$  and OH groups antisymmetric stretching ( $\nu_a$ ) movements [20]. In addition, the absorption band centered at 2050  $\text{cm}^{-1}$  is characteristic of motions from the  $\text{NH}_3$  group, belonging to the L-thr molecule [36]. Complementarily, around 1651 and 1626  $\text{cm}^{-1}$ , there is a doublet associated with the carboxyl-group  $\nu_a$ -vibrations [30]. On the other hand, in the spectral range between 1480 and 1380  $\text{cm}^{-1}$ , the bands corresponding to the antisymmetric deformations ( $\delta_a$ ) of the methyl group are located [34]. The low wavenumber bands correspond to the  $\text{CO}_2$ -group deformation ( $\delta$ ) vibrations with contributions from the COH groups, and are arranged at 769, 747, 701, and 560  $\text{cm}^{-1}$  [22,33].

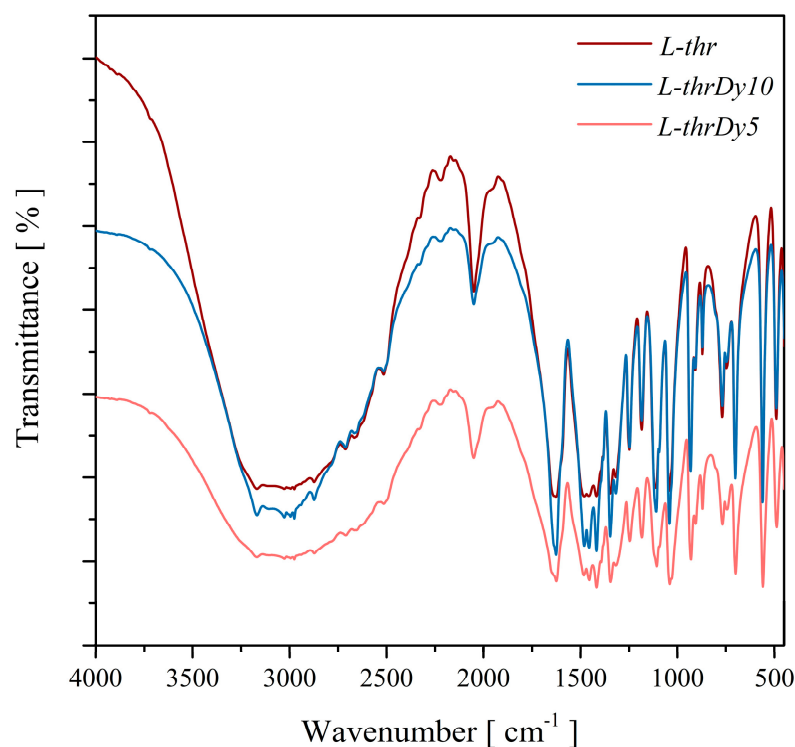


**Figure 6.** FT-IR absorption spectra of L-thr, L-thrDy5, and L-thrDy10 powdered crystals.

### 3.5. Raman Spectroscopy Studies

Figure 7a presents the Raman spectra recorded at room temperature for L-thr, L-thrDy5, and L-thrDy10 powdered crystals in the spectral region of 40–250  $\text{cm}^{-1}$ . Generally, bands below 200  $\text{cm}^{-1}$  in amino acids are associated with vibrational modes corresponding to intermolecular interactions that couple with hydrogen bonds present in the crystal (lattice modes), as also observed for the amino acids  $\beta$ -Alanine, glycine, and histidine in Raman spectroscopy studies of coordination compounds and organics salts [37–39]. In this interval, the bands centered around 46, 72, 99, 105, 131, and 156  $\text{cm}^{-1}$  for the L-thr sample are slightly shifted to major wavenumbers compared to samples without  $\text{Dy}^{3+}$  ions. Additionally, variations in intensity are observed for different bands throughout the Raman spectrum. These spectral changes are attributed to the presence of  $\text{Dy}^{3+}$  ions in the L-thr matrix. Furthermore, as previously discussed, the insertion of the lanthanide ion into the lattice exerts a pressure effect on the unit cell, indirectly affecting hydrogen bonds. Complementarily, the variation in scattering intensity between the samples can be explained by defects generated in the crystalline structure due to the introduction of impurities, as noted in other studies [40,41].

In the three crystals, the vibrational modes observed between the 200 and 1700  $\text{cm}^{-1}$  range are associated with intramolecular vibrations corresponding to the deformation ( $\delta$ ) and stretching ( $\nu$ ) motions of the L-thr molecular structure (Figure 7a,b) [42–45]. For the L-thr crystal, the bands centered around 215, 380, 568, and 876  $\text{cm}^{-1}$  were assigned to  $\tau(\text{NH}_3)$ —torsion,  $\delta(\text{CCO})$ —bending,  $\rho(\text{CH}_3)$ —rocking, and  $\delta(\text{CO}_2)$ —bending motions, respectively [36]. However, in the L-thrDy5 and L-thrDy10 crystals, these modes undergo a slight red shift due to the presence of  $\text{Dy}^{3+}$  ions in the crystal structure. Based on these data, it is observed that the concentration of impurities inserted into the L-thr matrix did not cause significant changes, supporting the hypothesis that  $\text{Dy}^{3+}$  ions occupy interstitial positions within the L-thr crystal. Nevertheless, a high-intensity band is observed around 564  $\text{cm}^{-1}$  for the L-thrDy5 and L-thrDy10 crystals, associated with the  $\tau(\text{CO}_2)$  motion [30,46]. This same mode was also observed for the L-thr crystal but with a lower scattering intensity.

It is possible that the  $\text{Dy}^{3+}$  ions interact with the L-thr molecule through hydrogen bonds with the functional groups of the amino acid, favoring some molecular vibrations.

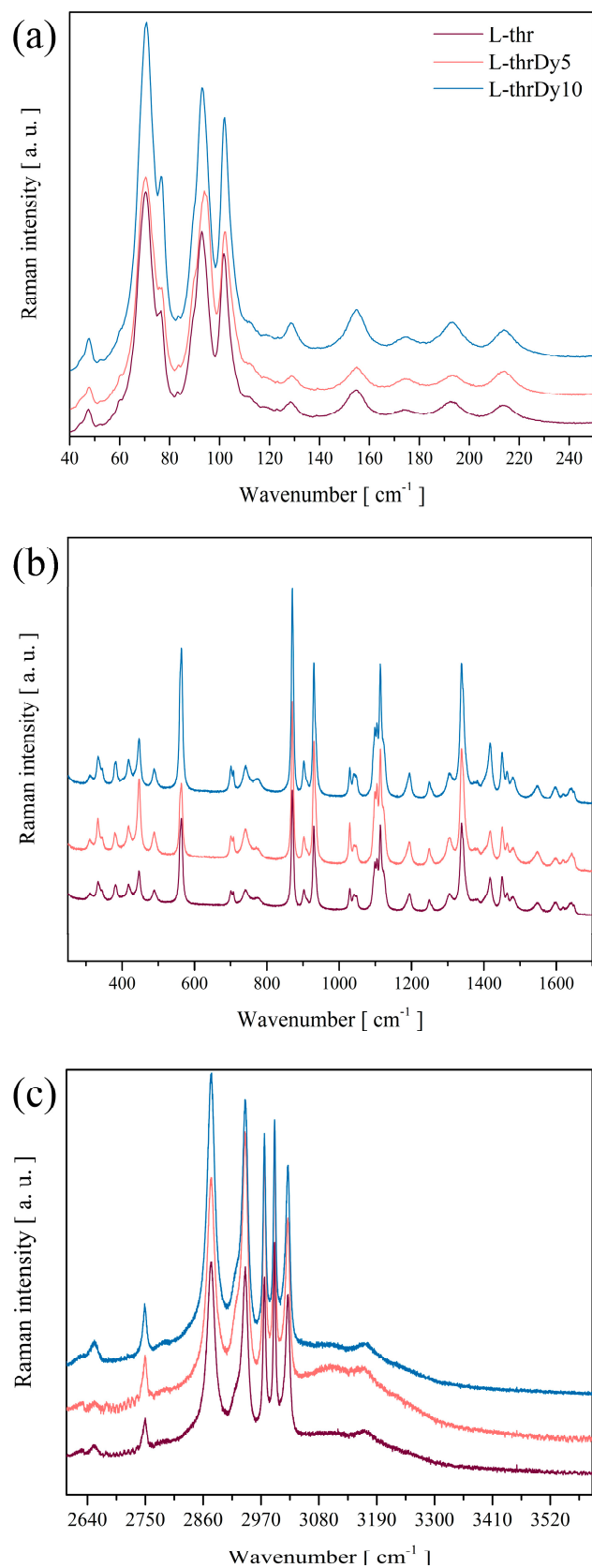


**Figure 7.** Raman spectra of L-thr, L-thrDy5, and L-thrDy10 crystals in the (a) 40–250  $\text{cm}^{-1}$ , (b) 250–1700  $\text{cm}^{-1}$ , and (c) 2600–3600  $\text{cm}^{-1}$ .

Still in this region, the majority, only changes in intensity were observed in almost all bands due to the presence of  $\text{Dy}^{3+}$  impurities in the L-thr matrix. The vibrational modes associated with  $\text{CH}_2$  group,  $\delta(\text{CH}_2)$ , are located around 870, 929, 1113, 1249, 1340, and  $1451\text{ cm}^{-1}$  [47]. Furthermore, the highest intensity band centered at  $1338\text{ cm}^{-1}$  was designated as a CH-group rocking,  $\rho(\text{CH})$  [48]. The vibrational modes in the range between 1500 and  $1700\text{ cm}^{-1}$  are assigned to  $\nu(\text{C}=\text{O})$  and  $\delta(\text{NH}_3)$  vibrations, according to the literature [43].

In the region of high wavenumber recorded between 2600 and  $3600\text{ cm}^{-1}$ , ten vibrational modes are presented for L-thr, L-thrDy5, and L-thrDy10 crystals. The bands located in this range are characteristic of stretching movements from the methyl and amine groups [33,49].

For comparative purposes, the FT-IR and Raman spectra of the precursor compound ( $\text{Cl}_3\text{Dy}\cdot 5\text{H}_2\text{O}$ ) associated with  $\text{Dy}^{3+}$  ion impurities were measured, as presented in Figure S1 of the Supplementary Material. In summary, five distinct vibrational modes were observed: stretching modes of  $\nu_a(\text{H}_2\text{O})$  and  $\nu_s(\text{H}_2\text{O})$  (above  $3000\text{ cm}^{-1}$ ),  $\delta(\text{H}_2\text{O})$  ( $1600\text{--}1800\text{ cm}^{-1}$ ),  $\nu(\text{Cl}\text{--}\text{Cl})$  ( $600\text{--}800\text{ cm}^{-1}$ ), and  $\nu(\text{Dy}\text{--}\text{Cl})$  ( $600\text{--}400\text{ cm}^{-1}$ ) [50].

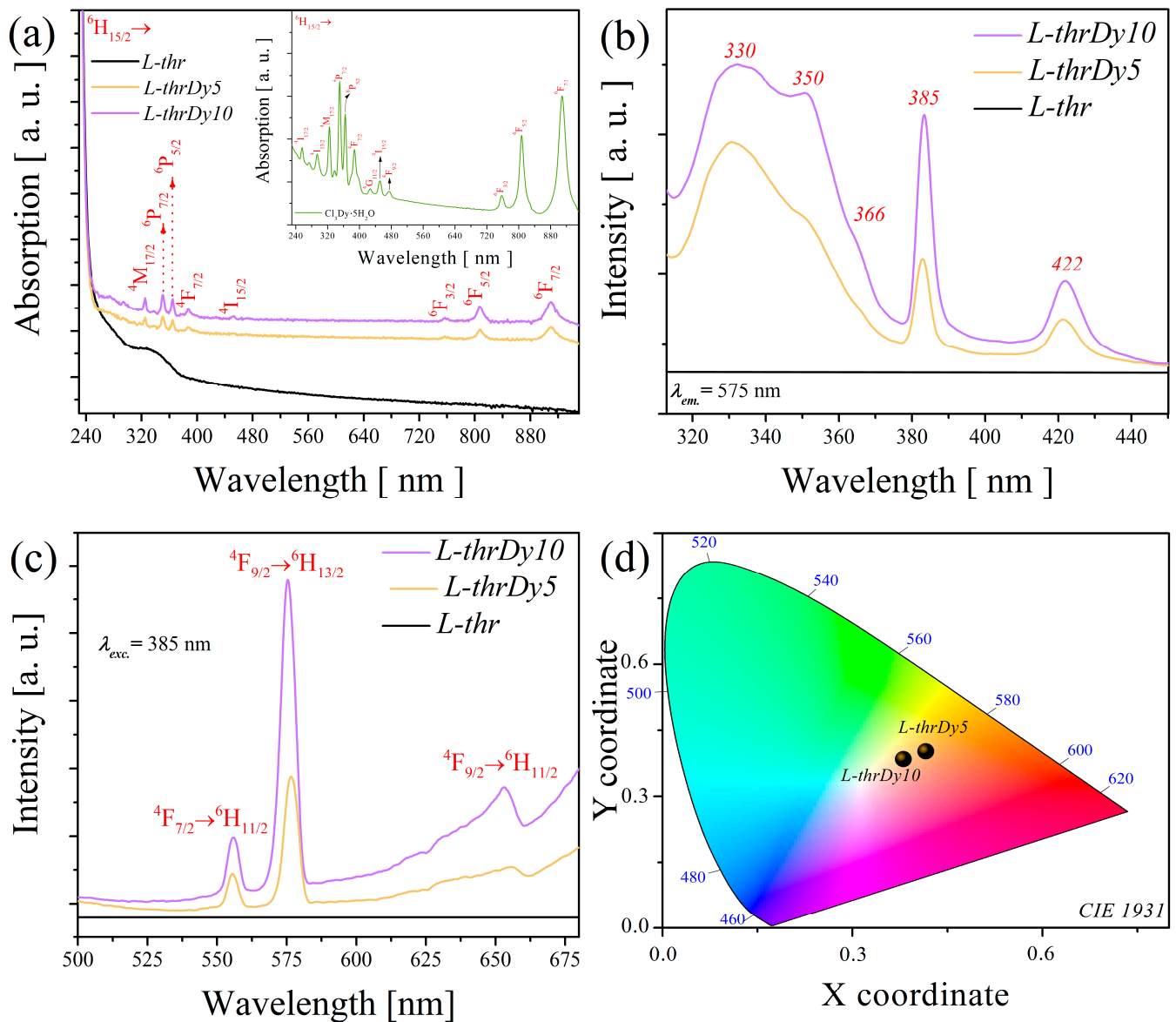
### 3.6. Optical Absorption and Photoluminescence Analysis

Figure 8a shows the optical absorption spectra recorded in the spectral range from 230 to 950 nm for L-thr, L-thrDy5, and L-thrDy10 crystals. As observed, the L-thr sample does not exhibit any electronic transition bands in the ultraviolet–visible region, except for a low-intensity shoulder at 330 nm, characteristic of amino acid compounds. This evidence confirms the optical transparency of the L-thr crystal, making it suitable as a host matrix for ionic doping and the introduction of impurities aimed at light emission. In contrast, the L-thrDy5 and L-thrDy10 crystals exhibit several absorption bands with intensities that increase with the concentration of  $\text{Dy}^{3+}$  ions in the L-thr matrix. All bands are associated with electronic transitions from the  ${}^6\text{H}_{15/2}$  ground state to various excited states. The optical spectra consist of eight absorption bands centered around 327, 352, 366, 389, 453, 757, 808, and 914 nm, corresponding to transitions  ${}^4\text{M}_{17/2}$ ,  ${}^6\text{P}_{7/2}$ ,  ${}^6\text{P}_{5/2}$ ,  ${}^4\text{F}_{7/2}$ ,  ${}^4\text{I}_{15/2}$ ,  ${}^6\text{F}_{3/2}$ ,  ${}^6\text{F}_{5/2}$ , and  ${}^6\text{F}_{7/2}$  [51–54], respectively. These transitions originate from the interaction of  $\text{Dy}^{3+}$  ions with the L-thr crystal lattice. Furthermore, the inset of Figure 8a shows the absorption spectrum of the compound  $\text{Cl}_3\text{Dy}\cdot 5\text{H}_2\text{O}$  with all band designations performed. Comparing the spectra involving the  $\text{Dy}^{3+}$  ions, it is observed that in the one associated with the precursor compound, more bands are detected; however, when interacting with the L-thr matrix, some are favored and others are suppressed, due to the influence of the crystal field on the structure.

Figure 8b shows the excitation spectra monitored around 575 nm for pure L-thr crystals and those containing  $\text{Dy}^{3+}$  impurities in the 310–450 nm spectral range. The large band located around 315 to 375 nm is associated with the overlapped electronic transitions of the  $\text{Dy}^{3+}$  ion due to the de-excitation process  ${}^6\text{H}_{15/2} \rightarrow {}^4\text{M}_{17/2}$  (330 nm),  ${}^6\text{P}_{7/2}$  (350 nm), and  ${}^6\text{P}_{5/2}$  (366 nm) [55]. The two peaks near 385 and 422 nm correspond to the excited state transitions  ${}^4\text{F}_{7/2}$  and  ${}^4\text{I}_{15/2}$ , respectively [56]. As observed, the intensities of all the excitation bands increase with the presence of  $\text{Dy}^{3+}$  ions. Additionally, no excitation peak with these characteristics was observed for the pure L-thr crystal.

Complementarily, the emission spectra under 385 nm excitation for L-thr, L-thrDy5, and L-thrDy10 crystals are shown in Figure 8c. For crystals containing  $\text{Dy}^{3+}$  ions, three bands located around 554, 575, and 662 nm were observed, associated with light emission in the green ( ${}^4\text{F}_{7/2} \rightarrow {}^6\text{H}_{11/2}$ ), yellow ( ${}^4\text{F}_{9/2} \rightarrow {}^6\text{H}_{13/2}$ ), and red ( ${}^4\text{F}_{9/2} \rightarrow {}^6\text{H}_{11/2}$ ) regions, respectively [57,58]. The electronic transition  ${}^4\text{F}_{9/2} \rightarrow {}^6\text{H}_{13/2}$ , corresponding to yellow light emission, is hypersensitive ( $\Delta L = 2$ ,  $\Delta J = 2$ ) to the host environment into which the  $\text{Dy}^{3+}$

ions are inserted [59]. This explains the small difference observed between the positions of the bands for the L-thrDy5 and L-thrDy10 crystals. It is likely that the  $Dy^{3+}$  impurities introduced into the L-thr matrix interact with the main molecule through the functional groups present in the amino acid, such as hydroxyl and carboxyl groups, resulting in a direct influence of the crystal lattice on the electronic transitions of the  $Dy^{3+}$  ions. Moreover, the intensity of the bands is proportional to the concentration of  $Dy^{3+}$  ions added to the L-thr lattice. As with the excitation spectrum, no band corresponding to the excitation source was observed for the pure L-thr crystal.



the CIE 1931 diagram obtained for L-thrDy5 and L-thrDy10 crystals. As observed, both crystals presented different chromaticity coordinates due to the varying concentrations of Dy<sup>3+</sup> ions in the L-thr matrix. The L-thrDy5 crystal exhibited values of  $x = 0.4156$  and  $y = 0.4023$ , which, when combined, are associated with the emission of yellow-orange light. Similarly, for the L-thrDy10 crystal, the values of  $x = 0.3803$  and  $y = 0.3845$  were obtained, corresponding to the emission of yellow light close to white.

Using the corresponding CIE chromaticity coordinates obtained for the L-thrDy5 and L-thrDy10 crystals, it was possible to estimate the CCT by McCamy's mathematical relationship [61]:

$$\text{CCT} = -449n^3 + 3525n^2 - 6823.3n + 5520.33 \quad (2)$$

where  $n = (x - 0.3320)/(y - 0.1858)$ . Substituting  $(x, y) = (0.4156, 0.4023)$  for the L-thrDy5 crystal and  $(0.3803, 0.3845)$  for the L-thrDy10 crystal, the CCT values calculated were around 3385.5 and 4063.9 K, respectively. The extracted CCT values indicate that the crystals present a neutral light comfortable to the human eye. Based on the spectroscopic data obtained, L-thrDy5 and L-thrDy10 crystals can be considered promising candidates for applications in modern optical devices, due to their properties of light emission in the visible region and their CCT.

#### 4. Conclusions

In this paper, L-thr crystals with varying concentrations of dysprosium were successfully grown using the solvent slow evaporation method. PXRD measurements confirmed the crystalline nature of the samples and the  $P2_12_12_1$ -space group, which belongs to the orthorhombic symmetry. Furthermore, it was observed that the volume of the L-thr unit cell underwent structural expansion with the increase in Dy<sup>3+</sup> ion concentration in the crystal lattice. Dy<sup>3+</sup> ions likely occupy interstitial spaces within the crystal lattice, as the L-thr unit cell has a void volume of 40.33 Å<sup>3</sup> (7.42%), allowing these impurities to occupy void positions and interact with the main molecule through intermolecular forces. Furthermore, analysis using the Hirshfeld surface suggests that the cations embedded in the matrix interact with the primary molecule through contacts involving the COOH, NH<sub>3</sub>, or OH groups. FT-IR and Raman spectra revealed that the impurities were introduced interstitially into the host matrix, interacting with the main molecule through low-energy secondary bonds. The thermal stability of the L-thr amino acid slightly increased with the insertion of Dy<sup>3+</sup> ions into the samples. Optical analysis in the UV-Vis region showed eight absorption bands in the L-thr crystalline matrix, attributed to transitions from the <sup>6</sup>H<sub>15/2</sub> ground state to various excited states of Dy<sup>3+</sup> ions. The L-thrDy5 and L-thrDy10 crystals, under excitation from a source of electromagnetic radiation at around 385 nm, produced light emission with three bands located at approximately 554, 575, and 662 nm. Additionally, it was observed that increasing the concentration of Dy<sup>3+</sup> impurities resulted in increased intensity of the emission bands. The CIE diagram indicated that L-thr samples containing Dy<sup>3+</sup> ions can produce light near the white region, with the coordinates of the sample containing 10% wt of Dy<sup>3+</sup> located closer to the ideal white. These data suggest that L-thrDy5 and L-thrDy10 crystals are promising candidates for applications in optical devices.

**Supplementary Materials:** The following supporting information can be downloaded at: <https://www.mdpi.com/article/10.3390/qubs9010003/s1>, Figure S1: Experimental (a) FT-IR and (b) Raman spectra recorded at room conditions for the Cl3Dy.5H<sub>2</sub>O compound.

**Author Contributions:** Conceptualization, J.G.d.O.N., O.C.d.S.N. and J.A.O.R.; methodology, J.G.d.O.N., O.C.d.S.N. and J.R.V.; software, J.G.d.O.N., O.C.d.S.N. and J.R.V.; validation, J.G.d.O.N., O.C.d.S.N., J.A.O.R., A.S., F.P., F.F.d.S. and A.O.d.S.; formal analysis, J.G.d.O.N., O.C.d.S.N., J.A.O.R., J.R.V., A.S., F.P., F.F.d.S. and A.O.d.S.; investigation, J.G.d.O.N., O.C.d.S.N. and J.R.V.; resources, F.F.d.S. and A.O.d.S.; data curation, J.G.d.O.N., O.C.d.S.N., J.A.O.R., J.R.V., A.S., F.P., F.F.d.S. and A.O.d.S.; writing—original draft preparation, J.G.d.O.N., O.C.d.S.N. and J.A.O.R.; writing—review and editing, A.S., F.P., F.F.d.S. and A.O.d.S.; visualization, J.G.d.O.N., O.C.d.S.N. and J.R.V.; supervision, A.S., F.P., F.F.d.S. and A.O.d.S.; project administration, F.F.d.S. and A.O.d.S.; funding acquisition, F.F.d.S. and A.O.d.S. All authors have read and agreed to the published version of the manuscript.

**Funding:** This research was funded by the Fundação de Amparo à Pesquisa e ao Desenvolvimento Científico e Tecnológico do Maranhão (FAPEMA), grant number BPD-12643/22; the Coordenação de Aperfeiçoamento de Pessoal de Nível Superior (CAPES), grant number 001; and the National Council for Scientific and Technological Development (CNPq), grant numbers 312926/2020-0, and 317469/2021-5.

**Data Availability Statement:** Data are contained within the article.

**Acknowledgments:** All authors thank the Postgraduate Program in Materials Science at the Federal University of Maranhão and the Institute of Exact and Natural Sciences of the Federal University of Pará.

**Conflicts of Interest:** The authors declare that they have no known competing financial interests or personal relationships that could have appeared to influence the work reported in this paper.

## References

1. Bhagavannarayana, G.; Parthiban, S.; Meenakshisundaram, S. An Interesting Correlation between Crystalline Perfection and Second Harmonic Generation Efficiency on KCl- and Oxalic Acid-Doped ADP Crystals. *Cryst. Growth Des.* **2008**, *8*, 446–451. [[CrossRef](#)]
2. Kushwaha, S.K.; Shakir, M.; Maurya, K.K.; Shah, A.L.; Wahab, M.A.; Bhagavannarayana, G. Remarkable Enhancement in Crystalline Perfection, Second Harmonic Generation Efficiency, Optical Transparency, and Laser Damage Threshold in Potassium Dihydrogen Phosphate Crystals by L-Threonine Doping. *J. Appl. Phys.* **2010**, *108*, 033506. [[CrossRef](#)]
3. Neto, J.G.O.; Viana, J.R.; Lopes, J.B.O.; Lima, A.D.S.G.; Sousa, M.L.; Lage, M.R.; Stoyanov, S.R.; Lang, R.; Santos, A.O. Crystal Growth, Crystal Structure Determination, and Computational Studies of a New Mixed  $(\text{NH}_4)_2\text{Mn}_1\text{-XZn}(\text{SO}_4)_2(\text{H}_2\text{O})_6$  Tutton Salt. *J. Mol. Model.* **2022**, *28*, 341. [[CrossRef](#)]
4. Oliveira Neto, J.G.D.; Marques, J.V.; Silva, G.; Antonelli, E.; Ayala, A.P.; Santos, A.O.; Lang, R. Mixed  $(\text{NH}_4)_2\text{Mn}_{0.47}\text{Cu}_{0.53}(\text{SO}_4)_2(\text{H}_2\text{O})_6$  Tutton Salt: A Novel Optical Material for Solar-Blind Technology. *Opt. Mater.* **2024**, *157*, 116400. [[CrossRef](#)]
5. Himamaheswara Rao, V.; Syam Prasad, P.; Mohan Babu, M.; Venkateswara Rao, P.; Satyanarayana, T.; Luís, F.S.; Veeraiyah, N. Spectroscopic Studies of  $\text{Dy}^{3+}$  Ion Doped Tellurite Glasses for Solid State Lasers and White LEDs. *Spectrochim. Acta Part A Mol. Biomol. Spectrosc.* **2018**, *188*, 516–524. [[CrossRef](#)]
6. Amor, C.O.; Kais, E.; Virlan, C.; Pui, A.; Elaloui, E. Effect of Dysprosium Ion ( $\text{Dy}^{3+}$ ) Doping on Morphological, Crystal Growth and Optical Properties of  $\text{TiO}_2$  Particles and Thin Films. *Phys. B Condens. Matter* **2019**, *560*, 67–74. [[CrossRef](#)]
7. Dorenbos, P. The  $4f_n \leftrightarrow 4f_{n-1} 5d$  Transitions of the Trivalent Lanthanides in Halogenides and Chalcogenides. *J. Lumin.* **2000**, *91*, 91–106. [[CrossRef](#)]
8. Ozturk, B.; Soyulu, G.S.P. Promoting Role of Transition Metal Oxide on  $\text{ZnTiO}_3\text{-TiO}_2$  Nanocomposites for the Photocatalytic Activity under Solar Light Irradiation. *Ceram. Int.* **2016**, *42*, 11184–11192. [[CrossRef](#)]
9. Chimalawong, P.; Kirdsiri, K.; Kaewkhao, J.; Limsuwan, P. Investigation on the Physical and Optical Properties of  $\text{Dy}^{3+}$  Doped Soda-Lime-Silicate Glasses. *Procedia Eng.* **2012**, *32*, 690–698. [[CrossRef](#)]
10. Alexander, D.; Thomas, K.; Manju Gopinath, R.J.; Joy, M.; Biju, P.R.; Unnikrishnan, N.V.; Joseph, C. Novel White Light Emitting Dysprosium Oxalate Nanocrystals: Competing Luminescence Quenching by the Features of Dy-Oxalate Layered Structure. *J. Alloys Compd.* **2019**, *804*, 252–261. [[CrossRef](#)]
11. Jayachandiran, M.; Kennedy, S.M.M. Synthesis and Optical Properties of  $\text{Ba}_3\text{Bi}_2(\text{PO}_4)_4:\text{Dy}^{3+}$  Phosphors for White Light Emitting Diodes. *J. Alloys Compd.* **2019**, *775*, 353–359. [[CrossRef](#)]
12. Huang, W.; Liu, Q.; Li, X.; Zhu, Q.; Wang, L.; Zhang, Q.  $\text{Dy}^{3+}$ -Doped  $\text{BaLaMgSbO}_6$  Double Perovskite Highly Efficient White Phosphor. *Ceram. Int.* **2019**, *45*, 15624–15628. [[CrossRef](#)]

13. Fleck, M.; Petrosyan, A.M. *Salts of Amino Acids*; Springer International Publishing: Cham, Switzerland, 2014; ISBN 978-3-319-06298-3.
14. Rajyalakshmi, S.; Ramachandra Rao, K.; Brahmaji, B.; Samatha, K.; Visweswara Rao, T.K.; Ramakrishna, Y. Investigations on Structural and Photoluminescence Mechanism of Cerium Doped L-Histidine Hydrochloride Mono Hydrate Single Crystals for Optical Applications. *J. Mol. Struct.* **2017**, *1129*, 231–238. [[CrossRef](#)]
15. Rajyalakshmi, S.; Ramachandra Rao, K.; Brahmaji, B.; Samatha, K.; Visweswara Rao, T.K.; Bhagavannarayana, G. Optical Investigations on Tb<sup>3+</sup> Doped L-Histidine Hydrochloride Mono Hydrate Single Crystals Grown by Low Temperature Solution Techniques. *Opt. Mater.* **2016**, *54*, 74–83. [[CrossRef](#)]
16. Ramachandra Rao, K.; Rajyalakshmi, S.; Kamal, C.S.; Brahmaji, B.; Jasinski, J.B.; Visweswara Rao, T.K. Unique Optical Properties of Eu<sup>3+</sup> Doped L-Histidine Hydrochloride Mono Hydrate Single Crystals from Low Temperature Growth Technique. *Spectrochim. Acta Part A Mol. Biomol. Spectrosc.* **2017**, *176*, 52–57. [[CrossRef](#)] [[PubMed](#)]
17. Brahmaji, B.; Rajyalakshmi, S.; Satya, C.; Atla, V.; Veeraiyah, V.; Rao, K.V.; Rao, K.R. Optical Emissions of Ce<sup>3+</sup> Doped Sulphamic Acid Single Crystals by Low Temperature Unidirectional Growth Technique. *Opt. Mater.* **2017**, *64*, 100–105. [[CrossRef](#)]
18. Ramanadham, M.; Sikka, S.K.; Chidambaram, R. Structure Determination of Ls-Threonine by Neutron Diffraction. *Pramana* **1973**, *1*, 247–259. [[CrossRef](#)]
19. Kumar, M.R.S.; Ravindra, H.J.; Jayarama, A.; Dharmaprakash, S.M. Structural Characteristics and Second Harmonic Generation in L-Threonine Crystals. *J. Cryst. Growth* **2006**, *286*, 451–456. [[CrossRef](#)]
20. Araújo, R.L.; Vasconcelos, M.S.; Barboza, C.A.; Lima Neto, J.X.; Albuquerque, E.L.; Fulco, U.L. DFT Calculations of the Structural, Electronic, Optical and Vibrational Properties of Anhydrous Orthorhombic L-Threonine Crystals. *Comput. Theor. Chem.* **2019**, *1170*, 112621. [[CrossRef](#)]
21. Joshi, J.H.; Kanchan, D.K.; Jethva, H.O.; Joshi, M.J.; Parikh, K.D. Dielectric Relaxation, Protonic Defect, Conductivity Mechanisms, Complex Impedance and Modulus Spectroscopic Studies of Pure and L-Threonine-Doped Ammonium Dihydrogen Phosphate. *Ionics* **2018**, *24*, 1995–2016. [[CrossRef](#)]
22. Thilakavathi, G.; Arun Kumar, R.; Kumares, A.; Ravikumar, N. Growth and Characterization of L-Threonine Doped Thiourea Single Crystals: An Optical Material. *Mater. Res. Innov.* **2016**, *20*, 254–258. [[CrossRef](#)]
23. Toby, B.H. EXPGUI, a Graphical User Interface for GSAS. *J. Appl. Crystallogr.* **2001**, *34*, 210–213. [[CrossRef](#)]
24. Spackman, P.R.; Turner, M.J.; McKinnon, J.J.; Wolff, S.K.; Grimwood, D.J.; Jayatilaka, D.; Spackman, M.A. CrystalExplorer: A Program for Hirshfeld Surface Analysis, Visualization and Quantitative Analysis of Molecular Crystals. *J. Appl. Crystallogr.* **2021**, *54*, 1006–1011. [[CrossRef](#)] [[PubMed](#)]
25. Oliveira Neto, J.G.d.; Santos, R.S.; Abreu, K.R.; Silva, L.M.d.; Lang, R.; Santos, A.O.d. Temperature-Induced Phase Transformations in Tutton Salt K<sub>2</sub>Cu(SO<sub>4</sub>)<sub>2</sub>(H<sub>2</sub>O)<sub>6</sub>: Thermoanalytical Studies Combined with Powder X-Ray Diffraction. *Physchem* **2024**, *4*, 458–469. [[CrossRef](#)]
26. Santana, R.C.; Cunha, R.O.; Santos, M.G.; Ferreira, K.D.; Carvalho, J.F.; Calvo, R. Growth, EPR and Optical Absorption Spectra of L-Threonine Single Crystals Doped with Cu<sup>2+</sup> Ions. *J. Phys. Chem. Solids* **2007**, *68*, 586–593. [[CrossRef](#)]
27. de Oliveira Neto, J.G.; Viana, J.R.; Souza Júnior, M.V.; Queiroz, L.H.S.; Reis, A.S.; Lage, M.R.; Souto, E.B.; de Sousa, F.F.; dos Santos, A.O. Dichloro-Bis(Theophylline)-Copper(II) Complex: Characterization of the Physicochemical, Computational Pharmacokinetics, Molecular Docking, and Cytotoxicity as Potential Antitumoral Medicine. *Polyhedron* **2024**, *264*, 117234. [[CrossRef](#)]
28. Patterson, A.L. The Scherrer Formula for X-ray Particle Size Determination. *Phys. Rev.* **1939**, *56*, 978–982. [[CrossRef](#)]
29. Williamson, G.K.; Hall, W.H. X-ray Line Broadening from Filled Aluminium and Wolfram. *Acta Metall.* **1953**, *1*, 22–31. [[CrossRef](#)]
30. Oliveira Neto, J.G.; Silva Neto, O.C.; Pedrochi, F.; Steimacher, A.; Filho, J.G.S.; de Sousa, F.F.; Silva, L.M.; Santos, A.O. Structural, Vibrational, Thermal, and Optical Properties of L-Threonine Crystals Containing Ce<sup>3+</sup> Ions. *J. Mol. Struct.* **2022**, *1254*, 132316. [[CrossRef](#)]
31. Spackman, M.A.; Jayatilaka, D. Hirshfeld Surface Analysis. *CrystEngComm* **2009**, *11*, 19–32. [[CrossRef](#)]
32. de Oliveira Neto, J.G.; Souza Junior, M.V.; Ayala, A.P.; Nogueira, C.E.S.; Souto, E.B.; dos Santos, A.O.; de Sousa, F.F. Structural Design, H-Bonding Interactions, Vibrational Properties, Periodic-DFT Calculations, and Antibacterial Activity of a Nicotinamide Cocrystal Using Tetradecanoic Acid as a Cofomer. *Cryst. Growth Des.* **2024**, *24*, 9810–9823. [[CrossRef](#)]
33. de Oliveira Neto, J.G.; Marques, J.V.; da Silva Neto, O.C.; de Oliveira Carvalho, J.; da Silva, L.M.; Mendes, F.; Macêdo, A.A.M.; dos Santos, A.O. Investigation of the Structural, Thermal, and Spectroscopic Properties of L-Threonine Crystal Containing Eu<sup>3+</sup> Ions for Use in Visible Light-Emitting Devices. *J. Mater. Sci. Mater. Electron.* **2023**, *34*, 1705. [[CrossRef](#)]
34. Moitra, S.; Kar, T. Second Harmonic Generation of a New Nonlinear Optical Material L-Valine Hydrobromide. *J. Cryst. Growth* **2008**, *310*, 4539–4543. [[CrossRef](#)]
35. Vijayan, N.; Rajasekaran, S.; Bhagavannarayana, G.; Ramesh Babu, R.; Gopalakrishnan, R.; Palanichamy, M.; Ramasamy, P. Growth and Characterization of Nonlinear Optical Amino Acid Single Crystal: L-Alanine. *Cryst. Growth Des.* **2006**, *6*, 2441–2445. [[CrossRef](#)]

36. Guzzetti, K.A.; Brizuela, A.B.; Romano, E.; Brandán, S.A. Structural and Vibrational Study on Zwitterions of L-Threonine in Aqueous Phase Using the FT-Raman and SCRF Calculations. *J. Mol. Struct.* **2013**, *1045*, 171–179. [[CrossRef](#)]
37. Neto, J.G.O.; da Silva Filho, J.G.; Cruz, N.S.; de Sousa, F.F.; Filho, P.F.F.; Santos, A.O. Growth, Structural, Vibrational, DFT and Thermal Studies of Bis( $\beta$ -Alanine) Nickel(II) Dihydrate Crystals. *J. Phys. Chem. Solids* **2020**, *141*, 109435. [[CrossRef](#)]
38. Rodrigues, J.A.O.; Oliveira Neto, J.G.; Santos, C.C.; Nogueira, C.E.S.; de Sousa, F.F.; de Menezes, A.S.; dos Santos, A.O. Phase Changes of Tris(Glycinato)Chromium(III) Monohydrate Crystal Systematically Studied by Thermal Analyses, XRPD, FTIR, and Raman Combined with Ab Initio Calculations. *Spectrochim. Acta Part A Mol. Biomol. Spectrosc.* **2022**, *271*, 120883. [[CrossRef](#)]
39. Moura, G.M.; Carvalho, J.O.; Silva, M.C.D.; Façanha Filho, P.F.; Dos Santos, A.O. Structural, Vibrational and Thermal Characterization of Phase Transformation in l-Histidinium Bromide Monohydrate Single Crystals. *Mater. Chem. Phys.* **2015**, *165*, 150–155. [[CrossRef](#)]
40. Ganesh, V.; Riscob, B.; Maurya, K.K.; Rao, K.K.; Wahab, M.A.; Bhagavannarayana, G. Effect of L-Threonine Doping on Structural, Optical, Mechanical, Surface and Dielectric Properties of KDP Single Crystal. *Int. J. Pure Appl. Phys.* **2011**, *7*, 13–24.
41. Pacheco, T.S.; Ludwig, Z.M.C.; Sant'Anna, D.R.; Perpétuo, G.J.; Franco, C.J.; Paiva, E.C.; Ghosh, S. Growth and Vibrational Spectroscopy of  $K_2Li_yNi_xCo_{1-x}(SO_4)_2 \cdot 6H_2O$  ( $Y = 0.1; 0.2; 0.3; 0.4$ ) Crystals. *Vib. Spectrosc.* **2020**, *109*, 103093. [[CrossRef](#)]
42. Theras, J.E.M.; Kalaivani, D.; Jayaraman, D.; Joseph, V. Growth and Spectroscopic, Thermodynamic and Nonlinear Optical Studies of L-Threonine Phthalate Crystal. *J. Cryst. Growth* **2015**, *427*, 29–35. [[CrossRef](#)]
43. Borah, B.; Devi, T.G. Molecular Property Analysis of the Interacting State of L-Threonine and Metformin: An Experimental and Computational Approach. *J. Mol. Struct.* **2020**, *1221*, 128819. [[CrossRef](#)]
44. Gargaro, A.R.; Barron, L.D.; Hecht, L. Vibrational Raman Optical Activity of Simple Amino Acids. *J. Raman Spectrosc.* **1993**, *24*, 91–96. [[CrossRef](#)]
45. Oliveira Neto, J.G.; Cavalcante, L.A.; Gomes, E.S.; Dos Santos, A.O.; Sousa, F.F.; Mendes, F.; Macêdo, A.A.M. Crystalline Films of L-Threonine Complexed with Copper (II) Dispersed in a Galactomannan Solution: A Structural, Vibrational, and Thermal Study. *Polym. Eng. Sci.* **2020**, *60*, 71–77. [[CrossRef](#)]
46. Ramesh Kumar, G.; Gokul Raj, S. Growth and Physiochemical Properties of Second-Order Nonlinear Optical L-Threonine Single Crystals. *Adv. Mater. Sci. Eng.* **2009**, *2009*, 704294. [[CrossRef](#)]
47. Hernandez, B.; Pflger, F.; Adenier, A.; Nsangou, M.; Kruglik, S.G.; Ghomi, M. Energy Maps, Side Chain Conformational Flexibility, and Vibrational Features of Polar Amino Acids L-Serine and L-Threonine in Aqueous Environment. *J. Chem. Phys.* **2011**, *135*, 055101. [[CrossRef](#)]
48. Ci, D.D.; Filho, J.M. Polarized Raman Spectra and Infrared Analysis of Vibrational Modes in L-Threonine Crystals. *Braz. J. Phys.* **1998**, *28*, 19–24. [[CrossRef](#)]
49. Prazyan, T.L.; Zhuravlev, Y.N.; Golovko, O.V.; Obolonskaya, O.S. DFT-Study of Pressure-Induced Phase Transition in L-Threonine. *J. Mol. Struct.* **2019**, *1196*, 271–279. [[CrossRef](#)]
50. Socrates, G. *Infrared and Raman Characteristic Group Frequencies*; John Wiley & Sons: Hoboken, NJ, USA, 2004; ISBN 978-0-470-09307-8.
51. Azeem, P.A.; Balaji, S.; Reddy, R.R. Spectroscopic Properties of  $Dy^{3+}$  Ions in  $NaF-B_2O_3-Al_2O_3$  Glasses. *Spectrochim. Acta Part A Mol. Biomol. Spectrosc.* **2008**, *69*, 183–188. [[CrossRef](#)]
52. Yang, F.; Tu, C.; Wang, H.; Wei, Y.; You, Z.; Jia, G.; Li, J.; Zhu, Z.; Lu, X.; Wang, Y. Growth and Spectroscopy of  $Dy^{3+}$  Doped in  $ZnWO_4$  Crystal. *Opt. Mater.* **2007**, *29*, 1861–1865. [[CrossRef](#)]
53. Shivakumara, C.; Saraf, R.; Halappa, P. White Luminescence in  $Dy^{3+}$  Doped BiOCl Phosphors and Their Judd-Ofelt Analysis. *Dye. Pigment.* **2016**, *126*, 154–164. [[CrossRef](#)]
54. Sruthi, P.; Swapna, K.; Kumar, J.V.S.; Mahamuda, S.; Venkateswarulu, M.; Amer, D.; Sai, D.S.; Rao, A.S. Dysprosium Concentration-Dependent Fluorescent Properties of Antimony Lead Oxyfluoroborate Glasses. *Chem. Phys. Lett.* **2022**, *787*, 139210. [[CrossRef](#)]
55. Prasanna Kumar, J.B.; Ramgopal, G.; Vidya, Y.S.; Anantharaju, K.S.; Daruka Prasad, B.; Sharma, S.C.; Prashantha, S.C.; Nagaswarupa, H.P.; Kavyashree, D.; Nagabhushana, H. Green Synthesis of  $Y_2O_3:Dy^{3+}$  Nanophosphor with Enhanced Photocatalytic Activity. *Spectrochim. Acta Part A Mol. Biomol. Spectrosc.* **2015**, *149*, 687–697. [[CrossRef](#)]
56. Dhananjaya, N.; Nagabhushana, H.; Nagabhushana, B.M.; Chakradhar, R.P.S.; Shivakumara, C.; Rudraswamy, B. Synthesis, Characterization and Photoluminescence Properties of  $Gd_2O_3:Eu_3$  Nanophosphors Prepared by Solution Combustion Method. *Phys. B Condens. Matter* **2010**, *405*, 3795–3799. [[CrossRef](#)]
57. Sun, J.; Zhang, X.; Xia, Z.; Du, H. Synthesis and Luminescence Properties of Novel  $LiSrPO_4:Dy^{3+}$  Phosphor. *Mater. Res. Bull.* **2011**, *46*, 2179–2182. [[CrossRef](#)]
58. Dillip, G.R.; Kumar, G.B.; Bandi, V.R.; Hareesh, M.; Deva Prasad Raju, B.; Joo, S.W.; Bharat, L.K.; Yu, J.S. Versatile Host-Sensitized White Light Emission in a Single-Component  $K_3ZnB_5O_{10}:Dy^{3+}$  Phosphor for Ultraviolet Converted Light-Emitting Diodes. *J. Alloys Compd.* **2017**, *699*, 1108–1117. [[CrossRef](#)]

59. Liu, Y.; Yang, Z.; Yu, Q.; Li, X.; Yang, Y.; Li, P. Luminescence Properties of Ba<sub>2</sub>LiB<sub>5</sub>O 10:Dy<sup>3+</sup> Phosphor. *Mater. Lett.* **2011**, *65*, 1956–1958. [[CrossRef](#)]
60. Zhao, H.-D.; Yao, Y.-Y.; Sun, F.; Zhang, Q.; Yang, X.-H. Display the CIE 1931 Color Chromaticity Diagram with Digital Image Processing. In Proceedings of the 2013 International Conference on Optical Instruments and Technology: Optoelectronic Imaging and Processing Technology, Beijing, China, 17–19 November 2013; Volume 9045, p. 904510. [[CrossRef](#)]
61. McCamy, C.S. Correlated Color Temperature as an Explicit Function of Chromaticity Coordinates. *Color Res. Appl.* **1992**, *17*, 142–144. [[CrossRef](#)]

**Disclaimer/Publisher’s Note:** The statements, opinions and data contained in all publications are solely those of the individual author(s) and contributor(s) and not of MDPI and/or the editor(s). MDPI and/or the editor(s) disclaim responsibility for any injury to people or property resulting from any ideas, methods, instructions or products referred to in the content.